

# Vector Field-Guided Learning Predictive Control for Motion Planning of Mobile Robots with Unknown Dynamics

Yang Lu<sup>1</sup>, Weijia Yao<sup>2</sup>, *IEEE Member*, Yongqian Xiao<sup>1</sup>, Xin Xu<sup>1</sup>, *IEEE Senior Member*

**Abstract**—Safe maneuvering capability is critical for mobile robots in complex environments. However, robotic system dynamics are often time-varying, uncertain, or even unknown during the motion planning and control process. Therefore, many existing model-based reinforcement learning (RL) methods could not achieve satisfactory reliability in guaranteeing safety. To address this challenge, we propose a two-level Vector Field-guided Learning Predictive Control (VF-LPC) approach that guarantees safe maneuverability. The first level, the guiding level, generates safe desired trajectories using the designed kinodynamic guiding vector field, enabling safe motion in obstacle-dense environments. The second level, the Integrated Motion Planning and Control (IMPC) level, first uses the deep Koopman operator to learn a nominal dynamics model *offline* and then updates the model uncertainties *online* using sparse Gaussian processes (GPs). The learned dynamics and game-based safe barrier function are then incorporated into the learning predictive control framework to generate near-optimal control sequences. We conducted tests to compare the performance of VF-LPC with existing advanced planning methods in an obstacle-dense environment. The simulation results show that it can generate feasible trajectories quickly. Then, VF-LPC is evaluated against motion planning methods that employ model predictive control (MPC) and RL in high-fidelity CarSim software. The results show that VF-LPC outperforms them under metrics of completion time, route length, and average solution time. We also carried out path-tracking control tests on a racing road to validate the model uncertainties learning capability. Finally, we conducted real-world experiments on a Hongqi E-HS3 vehicle, further validating the VF-LPC approach’s effectiveness.

**Index Terms**—Collision avoidance, integrated planning and control, planning under uncertainty, reinforcement learning.

## I. INTRODUCTION

FOR motion planning and tracking control tasks, prior information or desired paths are often required to guide robots’ motion. As an effective and efficient method, guiding vector field (GVF) techniques have been recently studied to realize path-following or obstacle-avoidance tasks successfully for robots like fixed-wing airplanes [1], miniature air vehicles [2], quadcopters [3], etc. The guidance feature of GVF manifests as follows [4], [5]: **i)** simple kinematic models of robots are considered (such as single or double integrator models [6], [7]); **ii)** GVF provides guidance signals to be tracked by the inner-loop dynamic controller (see Fig. 1). Therefore, the guidance level (i.e., the design of the GVF) and the control level can be separately designed. Specifically, GVF is designed to converge its integral curves to the desired geometric paths

kinematically, and an effective robot dynamic controller is derived by exploiting the convergence properties of the integral curves under consideration of the robot’s dynamics. Therefore, obtaining sufficiently fast and precise dynamic controllers is important, as they must effectively respond to the kinematic controls (such as linear and angular velocities provided by GVFs). On the other hand, the dynamic controllers must take into account safety constraints. Considering the two aspects, it is imperative to propose an Integrated Motion Planning and Control (IMPC) approach. An IMPC approach generally considers the safety constraints and dynamics control, and generates controls directly transmitted to the low-level execution level. However, designing adaptive IMPC approaches for real-world robots with unknown dynamics is challenging, particularly in obstacle-dense scenarios.

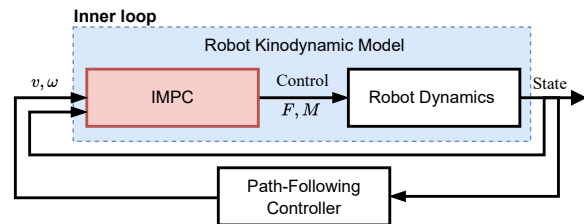


Fig. 1. The proposed control architecture. In this figure, the GVF-based path-following controller generates desired linear and angular velocities  $v$  and  $\omega$ ;  $F$  and  $M$  are forces and moments provided by the IMPC module.

Recent works on realizing reinforcement learning (RL) based IMPC were widely studied [8]–[10]. RL-based IMPC algorithms generally design proper reward functions based on priori information or desired paths to learn optimal policies. With the guidance information, existing endeavors primarily realize safe tracking control by designing reward functions encompassing state errors, control inputs, and safety terms. However, most of the studies assume that the desired paths are provided in advance, which is not valid when robots operate in different unstructured scenarios. When the desired path is constituted by a straight line from the starting point to the endpoint, it may traverse many obstacles in obstacle-dense environments. This increases the complexity of designing RL-based IMPC algorithms, posing challenges to achieving near-optimal performance. Therefore, providing guidance for RL methods is very important. Despite the above challenges, current RL-based IMPC has shown effectiveness and efficiency for robots with nonlinear system dynamics [8]–[10]. Letting RL-based IMPC approaches work as the IMPC structure in Fig. 1 is still promising if the above-discussed challenges can be well addressed. Namely, a GVF provides guidance for RL-based IMPC approaches.

There exist two categories of RL-based IMPC studies;

<sup>1</sup>Yang Lu, Yongqian Xiao, and Xin Xu are with the College of Intelligence Science and Technology, National University of Defense Technology, China luyang18@mail.sdu.edu.cn, xiaoyongqian18@nudt.edu.cn, xuxin\_mail@263.net. (Corresponding author: Xin Xu.)

<sup>2</sup>Weijia Yao is with the School of Robotics, Hunan University, China wjyao@hnu.edu.cn.

i.e., model-based and model-free ones. Obtaining a precise dynamic model is nontrivial due to internal factors such as system nonlinearity, and external factors such as uneven terrain, and slippery surfaces. The advantage of model-free RL methods lies in their independence from precise models, but they require many training samples for learning, resulting in much training time and very high risk. Efficient model-based RL approaches have shown their effectiveness in real-world applications [9], [10]. However, since the real-world robot dynamics are often uncertain or even unknown, model-based RL (MBRL) approaches struggle to achieve satisfactory reliability. This is due to: 1) The accuracy and adaptability of current data-driven modeling methods are insufficient. 2) The online learning efficiency of MBRL is too low to achieve fast convergence.

To realize motion planning of mobile robots with unknown dynamics in obstacle-dense scenarios, we propose a Vector Field-guided Learning Predictive Control (VF-LPC) approach. Specifically, the guiding level plans preliminary trajectories fast to avoid dense static obstacles. The optimal performance under the unknown system dynamics and the safety constraints from (suddenly appearing) moving obstacles are optimized by solving the Hamilton–Jacobi–Bellman (HJB) equation online in prediction horizons. In particular, we introduce a sparsification technique in the model compensation and finite-horizon actor-critic learning processes to improve the online efficiency and control performance. The contributions of this paper are summarized as follows:

- 1) By adding virtual obstacles, the modified and improved discrete-time composite vector field adopted by our VF-LPC approach can satisfy robot kinodynamic constraints. In addition, the modified vector field does not suffer from the deadlock problem, which usually exists in traditional composite vector fields. Moreover, VF-LPC can deal with (suddenly appearing) moving obstacles by introducing a game-based barrier function.
- 2) The VF-LPC approach can update online the uncertain dynamics of a fully data-driven model trained by the deep Koopman operator. It reduces the differences between the real and learned system dynamics models when the environment is time-varying or the system dynamics are learned inaccurately. Therefore, it improves the control performance and guarantees safety.
- 3) The VF-LPC approach can achieve near-optimal safety control for robots with unknown dynamics. The approach achieves higher computational efficiency and obtains more reliable solutions than advanced model predictive control (MPC) methods in solving nonlinear optimization problems.
- 4) Our proposed VF-LPC approach not only has theoretical guarantees but also has been demonstrated effective in practice since it has been validated by extensive simulations and experiments with a Hongqi E-HS3 vehicle in an environment with moving obstacles.

The remainder of this paper is organized as follows. Section II reviews the related works. Then Section III provides the preliminaries and problem formulation. The VF-LPC is intro-

duced in Section IV. Then, Section V presents the convergence results of VF-LPC. Section VI elaborates on the simulation and experimental validation. Finally, the conclusion is drawn in Section VII.

*Notation:* The notation  $\|x\|_Q^2$  represents  $x^\top Qx$ , where  $Q$  is a positive (semi-)definite matrix, and  $\|x\| = \sqrt{x^\top x}$ . The field of real numbers is denoted by  $\mathbb{R}$ . A diagonal matrix is denoted by  $\text{diag}\{\nu_1, \dots, \nu_n\}$ , where  $\nu_1, \dots, \nu_n \in \mathbb{R}$  are entries on the diagonal. Throughout this paper, we use the notation  $I$  to denote the identity matrix of suitable dimensions. The notations  $\otimes$  and  $\odot$  denote the Kronecker and Hadamard products, respectively.

## II. RELATED WORK

We first discuss several modeling methods and then present a literature review on popular MPC and MBRL approaches for the safety control of systems with uncertain dynamics.

*Data-driven modeling.* Current advanced data-driven modeling methods include least-squares [11], recurrent neural networks (NNs) [12], multi-layer perception (MLP) [13], neural networks [14], etc. As a linear operator, the Koopman operator-based modeling methods [15]–[18] can establish linear time-invariant system dynamics. Impressed by such a property, dynamic mode decomposition (DMD) [15], extended DMD (EDMD) [16], and kernel-based DMD [17] have received much attention in recent years. However, the modeling performance of the Koopman operator relies heavily on the observable function design. Consequently, approaches using NNs for automated observable function construction [19]–[21] were proposed to improve the modeling accuracy and have been validated to be effective through numerical simulations. To improve the modeling accuracy, Xiao et al. [22] proposed a deep Koopman operator method for identifying linear time-invariant vehicle dynamic models to track reference velocities. Additionally, vehicle control experiments were conducted in [23] to validate the effectiveness of the deep direct Koopman (DDK) method. Unlike these works, we further consider improving the online adaptability of offline-trained dynamics models by learning the uncertain dynamics of the offline-trained Koopman model.

*Sampling-based and optimization-based motion planning algorithms for robots with uncertain dynamics.* These algorithms necessitate the generation of paths/trajectories that conform to dynamic feasibility, collision avoidance, and uncertain dynamics. Lars et al. proposed a chance-constrained path planning method [24], which employs a probabilistic representation of uncertainty, thereby constraining the probability of collisions or deviations from specified regions within threshold limits. Several studies have integrated chance constraints with sampling-based Rapidly-exploring Random Trees (CC-RRT) methods, presenting efficient path planning capability in densely cluttered obstacle environments [25]. Gaussian processes (GPs) were employed for determining dynamically feasible paths and CC-RRT for establishing probabilistically feasible paths [26]. In [27], Kalman filtering was utilized for state estimation and risk-aware safety constraints arising from estimation errors were introduced into stochastic optimal

control problems. However, these approaches fail to guarantee optimality due to the lack of consideration of the robot's motion dynamics constraints. Utilizing model predictive control (MPC) to address motion planning under robot dynamic uncertainties typically involves objective functions incorporating Conditional Value-at-Risk (CVaR) measures [28], [29]. In summary, under unknown system dynamics, it is still challenging to efficiently realize safe and non-conservative control.

*MBRL for motion planning of robots with uncertain dynamics.* Some offline MBRL approaches complete complex tasks by using enormous training samples. Diehl et. al. tried to jointly solve multi-level problems of automated driving [30] in a simulator using offline collected real-world datasets. In [31], the new AEMCARL framework enables collision-free robot navigation in complex scenarios through adaptive modeling and learning. Besides these tasks, relevant efforts focus on specific tracking-avoiding tasks. In [9], our previous work devised an efficient online batch-mode RL approach to realize motion planning of uncertain vehicle dynamics. Zhang et al. [10] proposed receding-horizon RL with NN-based model compensation for realizing motion planning of intelligent vehicles. In this work, we focus on robot motion-planning tasks and design a new framework that further considers the unknown dynamics in obstacle-dense environments for realizing kinodynamic motion planning and control.

### III. PRELIMINARIES AND PROBLEM FORMULATION

This section presents a detailed preliminary for the composite vector field, which will be developed later in this paper for generating preliminary kinodynamic trajectories. Then, we review a data-driven deep Koopman-based system modeling method. The previously developed sparse GP can efficiently identify model uncertainties online, which is also reviewed here to identify the model uncertainties of the nominal model. Note that for one thing, GP can be used to identify the full system dynamics individually, but the long-horizon modeling accuracy is difficult to guarantee. To enhance the accuracy, one has to use flawless samples and fine-tune the hyperparameters, which can be computationally demanding. For another, the Koopman model may not accurately characterize the exact model, so estimating the uncertainty of model learning is essential. Therefore, to improve the accuracy, we propose to combine the Koopman model learning and the sparse GP. In particular, we employ online sparse GP to compensate for the inaccuracy and uncertainty associated with the offline-trained Koopman model, which will be introduced later in our methodology. Finally, we present the problem formulation for optimal motion planning under the fully data-driven system model containing uncertain dynamics.

#### A. Composite Vector Field

Consider the following ordinary differential equation

$$\dot{\xi} = \chi(\xi(t))$$

with the initial state  $\xi(0) \in \mathbb{R}^2$ , where  $\chi(\cdot)$  is continuously differentiable concerning  $\xi$ , and it is designed to be a guiding vector field for path following [32].

As shown in Fig. 2, the elements of the composite vector field are illustrated in detail. A reference path  $\mathcal{P}$  is provided initially and may be occluded by obstacles, and it is defined by

$$\mathcal{P} = \{\xi \in \mathbb{R}^2 : \phi(\xi) = 0\},$$

where  $\phi : \mathbb{R}^2 \rightarrow \mathbb{R}$  is twice continuously differentiable. For example, a circle path  $\mathcal{P}$  can be described by choosing  $\phi(x, y) = x^2 + y^2 - R^2$ , where  $R$  is the circle radius. To avoid collisions, Yao et al. [32] proposed a composite vector field for processing obstacle constraints. It involves a reactive boundary  $\mathcal{R}_i^t$  and a repulsive boundary  $\mathcal{Q}_i^t$ , i.e.,

$$\mathcal{R}_i^t = \{\xi \in \mathbb{R}^2 : \varphi_i(\xi, t) = 0\}, \mathcal{Q}_i^t = \{\xi \in \mathbb{R}^2 : \varphi_i(\xi, t) = c_i\},$$

where  $\varphi_i : \mathbb{R}^2 \times \mathbb{R} \rightarrow \mathbb{R}$  is twice continuously differentiable,  $i \in \mathcal{I} = \{1, 2, \dots, m\}$ ,  $m$  is the total number of obstacles, and  $c_i < 0$ . The repulsive boundary  $\mathcal{Q}_i^t$  is the boundary that tightly encloses the  $i$ -th obstacle at time  $t$  and a robot is forbidden to cross this boundary to avoid collision with the obstacle. The reactive boundary  $\mathcal{R}_i^t$  is larger than and encloses the repulsive boundary, and its interior is a region where a robot can detect an obstacle and become reactive. We use  $\text{ex}$  and  $\text{in}$  to denote the exterior and interior regions of a boundary, respectively. For example,  $\text{ex}\mathcal{Q}$  represents the exterior region of the repulsive boundary (see Fig. 2). An example of moving circular reactive and repulsive boundaries can be characterized by choosing  $\varphi_i(x, y; t) = (x - t)^2 + y^2 - R^2$  and letting  $|c_i| < R$ . In this case, the reactive and repulsive boundaries are large and small concentric circles moving along the  $x$ -axis as  $t$  increases, respectively.

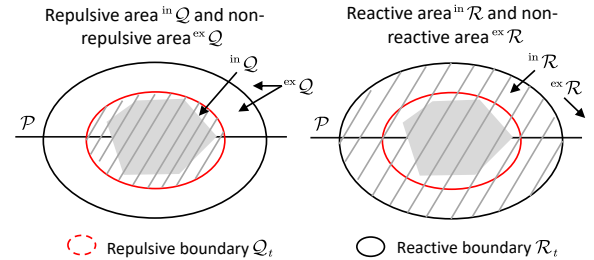


Fig. 2. Component illustration of the composite vector field [32]. The oblique lines construct a close area. The annulus area is the *sandwiched region*  $\mathcal{M}_s = \text{ex}\mathcal{Q} \cap \text{in}\mathcal{R}$ .

We denote the *path-following vector field* by  $\chi_{\mathcal{P}}$  and the *repulsive vector field* by  $\chi_{\mathcal{R}_i}$ , and they are defined below:

$$\begin{aligned} \chi_{\mathcal{P}}(\xi) &= \gamma_0 E \nabla \phi(\xi) - k_p \phi(\xi) \nabla \phi(\xi), \\ \chi_{\mathcal{R}_i}(\xi) &= \gamma_i E \nabla \varphi_i(\xi) - k_{r_i} \varphi_i(\xi) \nabla \varphi_i(\xi), \quad i \in \mathcal{I}, \end{aligned}$$

where  $E = \begin{bmatrix} 0 & -1 \\ 1 & 0 \end{bmatrix}$  is the rotation matrix of  $90^\circ$ ,  $\gamma_i \in \{1, -1\}$ ,  $i \in \mathcal{I} \cup \{0\}$ , determines the moving direction (clockwise or counterclockwise), and  $k_p, k_{r_i}$  are positive coefficients. The composite vector field is as follows [32]:

$$\chi(\xi) = \left( \prod_{i \in \mathcal{I}} \sqcup_{\mathcal{Q}_i}(\xi) \right) \hat{\chi}_{\mathcal{P}}(\xi) + \sum_{i \in \mathcal{I}} (\sqcap_{\mathcal{R}_i}(\xi) \hat{\chi}_{\mathcal{R}_i}(\xi)), \quad (1)$$

where  $\hat{(\cdot)}$  is the normalization notation (i.e., for a nonzero vector  $v \in \mathbb{R}^n$ ,  $\hat{v} = v/\|v\|$ ),  $\sqcup_{\mathcal{Q}}(\xi) = \frac{f_1(\xi)}{f_1(\xi) + f_2(\xi)}$ ,  $\sqcap_{\mathcal{R}}(\xi) =$



$\frac{f_2(\xi)}{f_1(\xi)+f_2(\xi)}$  are smooth *bump functions*, where  $f_1(\xi) = 0$  if  $\varphi(\xi) \leq c$  and  $f_1(\xi) = \exp\left(\frac{l_1}{c-\varphi(\xi)}\right)$  if  $\varphi(\xi) > c$ ,  $f_2(\xi) = \exp\left(\frac{l_2}{\varphi(\xi)}\right)$  if  $\varphi(\xi) < 0$  and  $f_2(\xi) = 0$  if  $\varphi(\xi) \geq 0$ , and  $l_1, l_2 > 0$  are coefficients for changing the decaying or increasing rate. Note that for simplicity, the subscripts  $i$  of related symbols have been omitted above. These smooth bump functions blend parts of different vector fields and create a composite vector field for path following and collision avoidance; for more details, see [32]. To understand the composite vector field intuitively, we illustrate the composite vector field (1) in Fig. 3. For  $\chi(\xi)$  in (1), it is equal to  $\hat{\chi}_{\mathcal{P}}(\xi)$ ,  $\sqcup_{\mathcal{Q}}(\xi)\hat{\chi}_{\mathcal{P}}(\xi) + \sqcap_{\mathcal{R}}(\xi)\hat{\chi}_{\mathcal{R}}(\xi)$ , and  $\hat{\chi}_{\mathcal{R}}(\xi)$  within the three regions  $^{\text{ex}}\mathcal{R}$ ,  $^{\text{ex}}\mathcal{Q} \cap ^{\text{in}}\mathcal{R}$ , and  $^{\text{in}}\mathcal{Q}$ , respectively.

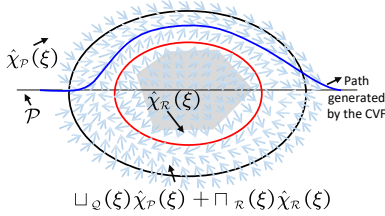


Fig. 3. An illustration of the composite vector field (1). We primarily illustrate the directions of the vector field in the vicinity of the path and directions partly within the interior region  $^{\text{in}}\mathcal{Q}$ .

The *singular sets* of  $\chi_{\mathcal{P}}$  and  $\chi_{\mathcal{R}_i}$ , denoted by  $\mathcal{C}_{\mathcal{P}}$  and  $\mathcal{C}_{\mathcal{R}_i}$ , respectively, are defined below:

$$\begin{aligned} \mathcal{C}_{\mathcal{P}} &= \{\xi \in \mathbb{R}^2 : \chi_{\mathcal{P}}(\xi) = 0\} = \{\xi \in \mathbb{R}^2 : \nabla\phi(\xi) = 0\}, \\ \mathcal{C}_{\mathcal{R}_i} &= \{\xi \in \mathbb{R}^2 : \chi_{\mathcal{R}_i}(\xi) = 0\} = \{\xi \in \mathbb{R}^2 : \nabla\varphi_i(\xi) = 0\}. \end{aligned}$$

The elements of singular sets are called *singular points*, where vector fields vanish. Due to the possible presence of singular points, special designs are required to solve the deadlock problem. When we employ the guiding vector field as high-level guiding signals, neglecting the kinodynamic constraints usually deteriorates the control performance. Therefore, in the subsequent sections, we will consider the kinodynamic constraints.

## B. Offline Deep Koopman Operator-based System Modeling

Consider the following continuous-time nonlinear system

$$\dot{x} = f(x, u), \quad (2)$$

where  $x \in \mathbb{R}^{n_x}$  denotes the system state,  $f : \mathbb{R}^{n_x} \times \mathbb{R}^{n_u} \rightarrow \mathbb{R}^{n_x}$  is the system transition function,  $u \in \Omega_u \subset \mathbb{R}^{n_u}$  denotes the control input, and  $\Omega_u$  is the control constraint set. Note that the explicit dependence on time is dropped unless needed for clarity. We assume that  $f(\cdot)$  is locally Lipschitz continuous.

The discrete-time Koopman operator of (2) can be described as follows:

$$\Upsilon_{\infty}(x_{k+1}) = (\mathcal{K}\Upsilon_{\infty})(x_k, u_k), \quad (3)$$

where  $\mathcal{K}$  is an infinite-dimensional linear Koopman operator in a Hilbert space  $\mathcal{H}$ , and  $\Upsilon_{\infty}$  is the observable function. In [23],  $\mathcal{K}$  is approximated by  $n_{\mathcal{K}}$ -order system dynamics by using deep neural networks, i.e.,

$$\Upsilon(x_{k+1}) = A\Upsilon(x_k) + Bu_k, \quad (4)$$

where  $A \in \mathbb{R}^{n_{\mathcal{K}} \times n_{\mathcal{K}}}$  and  $B \in \mathbb{R}^{n_{\mathcal{K}} \times n_u}$  are latent system matrices,  $\Upsilon(x_k) = [x_k^{\top}, \rho_e^{\top}(x_k)]^{\top}$  where  $\rho_e : \mathbb{R}^{n_x} \rightarrow \mathbb{R}^{n_{\rho_e}}$  denotes the encoder module.

## C. Sparse GP Regression for Online Compensation

Next, we will review a sparse GP regression method called FITC [33], which reduces computational complexity by selecting inducing samples and introduces a low-rank approximation of the covariance matrix, transforming the original GP model into an efficient one. It is briefly introduced in the following.

1) *The formulation of full GP Regression:* An independent training set is composed of state vectors, i.e.,  $\mathbf{z} = [z_1, z_2, \dots, z_n]^{\top} \in \mathbb{R}^{n \times n_z}$  and the corresponding output vectors  $\mathbf{y} = [y_1, y_2, \dots, y_n]^{\top} \in \mathbb{R}^{n \times n_y}$ . In [34], the mean and variance functions of each output dimension  $a \in \{1, \dots, n_y\}$  at a test point  $z = [x^{\top}, u^{\top}]^{\top}$  are computed by

$$\begin{aligned} m_d^a &= K_{zz}^a (K_{zz}^a + \sigma_a^2 I)^{-1} [\mathbf{y}]_a, \\ \Sigma_d^a &= K_{zz}^a - K_{zz}^a (K_{zz}^a + \sigma_a^2 I)^{-1} K_{zz}^a, \end{aligned} \quad (5)$$

where  $\sigma_a$  is the variance,  $K_{zz}^a = k^a(\mathbf{z}, \mathbf{z}) \in \mathbb{R}^{n_z \times n_z}$  is a Gram matrix containing variances of the training samples. Correspondingly,  $K_{zz}^a = (K_{zz}^a)^{\top} = k^a(z, \mathbf{z})$  denotes the variance between a test sample and training samples, and  $K_{zz}^a = k^a(z, z)$  represents the covariance,  $k^a(\cdot, \cdot)$  is the squared exponential kernel function and is defined as follows:

$$k^a(z_i, z_j) = \sigma_{f,a}^2 \exp(-1/2 (z_i - z_j)^{\top} L_a^{-1} (z_i - z_j)), \quad (6)$$

where  $\sigma_{f,a}^2$  is the signal variance and  $L_a = \ell^2 I$ . Here  $\sigma_{f,a}$  and  $\ell$  are hyperparameters of the covariance function.

2) *Sparse GP Regression:* Given an inducing dictionary set  $\{\mathbf{z}_{\text{ind}}, \mathbf{y}_{\text{ind}}\}$  with  $n_{\text{ind}}$  samples from  $\{\mathbf{z}, \mathbf{y}\}$ , the prior hyperparameters can be optimized by maximizing the marginal log-likelihood of the observed samples. In [33], the mean and variance functions of a full GP are approximated by using inducing targets  $\mathbf{y}_{\text{ind}}$ , inputs  $\mathbf{z}_{\text{ind}}$ , i.e.,

$$\begin{aligned} \tilde{m}_d^a(z) &= Q_{zz}^a (Q_{zz}^a + \Lambda)^{-1} [\mathbf{y}]_a, \\ \tilde{\Sigma}_d^a(z) &= K_{zz}^a - Q_{zz}^a (Q_{zz}^a + \Lambda)^{-1} Q_{zz}^a, \end{aligned} \quad (7)$$

where  $\Lambda = K_{zz}^a - Q_{zz}^a + \sigma_a^2 I$  is diagonal and the notation  $Q_{\zeta\bar{\zeta}}^a := K_{\zeta\mathbf{z}_{\text{ind}}}^a (K_{\mathbf{z}_{\text{ind}}\mathbf{z}_{\text{ind}}}^a)^{-1} K_{\mathbf{z}_{\text{ind}}\bar{\zeta}}^a$ . Several matrices in (7) do not depend on  $z$  and can be precomputed, such that they only need to be updated when updating  $\mathbf{z}_{\text{ind}}$  or  $\mathcal{D}$  itself.

Finally, a multivariate GP is established by

$$d(z) \sim \mathcal{N}(\tilde{m}_d, \tilde{\Sigma}_d), \quad (8)$$

where  $\tilde{m}_d = [\tilde{m}_d^1, \dots, \tilde{m}_d^{n_y}]^{\top}$ , and  $\tilde{\Sigma}_d = \text{diag}\{\tilde{\Sigma}_d^1, \dots, \tilde{\Sigma}_d^{n_y}\}$ .

## D. Problem Formulation

### 1) Composite Vector Field with Kinodynamic Constraints:

The composite vector field acts as a local path planner and should satisfy the kinodynamic constraint, leading to the problem of Vector-Field-guided Trajectory Planning with Kinodynamic Constraint (VF-TPKC), which is formulated in

**Definition 1.** This problem is decomposed into two components. In the presence of obstacles obstructing the desired path, the planning method should ensure the safety of paths, i.e., avoiding collision with obstacles. Then, the issue of satisfying dynamic constraints arises, involving improvements upon the path planning method established in the first step.

**Remark 1.** The term “kinodynamic constraint” refers to the requirement that a robot will not collide with obstacles at different speeds. To address this issue, we have transformed it into the fulfillment of the maximum lateral acceleration.

**Definition 1.** (VF-TPKC) Design a continuously differentiable vector field  $\chi : \mathbb{R} \times \mathbb{R}^2 \rightarrow \mathbb{R}^2$  for  $\xi(t) = \chi(t, \xi(t))$  such that:

- 1) It achieves path-following and collision avoidance. In addition, the path-following error is bounded, and no deadlocks exist.
- 2) Given the robot’s velocities  $v_x, v_y$ , and the maximum centripetal acceleration  $a_{\max}$ , it holds that  $(v_x^2 + v_y^2)\kappa(t) \leq a_{\max}$  for  $t > 0$  and  $\kappa(t)$  is the curvature at time  $t$ .

A guiding vector field  $\chi : \mathbb{R} \times \mathbb{R}^2 \rightarrow \mathbb{R}^2$  is designed to generate a continuously differentiable reference path, which is obtained by

$$\Xi = \int_0^\infty \chi(\xi(t)) dt.$$

Subsequently, we employ a learning-based predictive control approach to track the desired trajectories and avoid dynamic obstacles at the same time.

2) *Optimal Motion Planning to Avoid Moving Obstacles:* Given the offline learned system (4), it is feasible to use it to design optimal controllers. However, the interaction environments may be time-varying, causing the system dynamics to be uncertain. We can rewrite the exact system dynamics as a data-driven Koopman model adding an uncertain part by

$$\Upsilon(x_{k+1}) = \underbrace{A\Upsilon(x_k) + Bu_k}_{f_{\text{nom}}(\Upsilon(x_k), u_k)} + B_s \underbrace{(g(\Upsilon(x_k), u_k) + w_k)}_{y_k}, \quad (9)$$

where the above model consists of a known nominal part  $f_{\text{nom}}$  and an additive term  $y_k$ , which lies within the subspace spanned by  $B_s$  [35]. We assume that the process noise  $w_k \sim \mathcal{N}(0, \Sigma^w)$  is independent and identically distributed (i.i.d.), with spatially uncorrelated properties, i.e.,  $\Sigma^w = \text{diag}\{\sigma_1^2, \dots, \sigma_{n_y}^2\}$ , where  $n_y$  denotes the dimension of  $y_k$ .

Assuming that the desired trajectory can be denoted by

$$\Upsilon(x_{r,k+1}) = A\Upsilon(x_{r,k}) + Bu_{r,k}, \quad (10)$$

the subtraction of Eq. (10) from Eq. (9) yields the following error model, i.e.,

$$\tilde{x}_{k+1} = A\tilde{x}_k + B\tilde{u}_k + B_s \underbrace{(g(\Upsilon(x_k), u_k) + w_k)}_{y_k}, \quad (11)$$

where  $\tilde{x}_k = \Upsilon(x_k) - \Upsilon(x_{r,k})$  is the error state,  $x_{r,k}$  is the reference state, and  $\tilde{u}_k = u_k - u_{r,k}$  is the control input.

We formally define the optimal motion planning (OMP) problem, which consists of two subproblems. The first subproblem is the tracking control problem. To formulate this

subproblem, we first define the value function as the cumulative discounted sum of the infinite-horizon costs:

$$V_\infty(\tilde{x}_k) = \sum_{\tau=k}^{\infty} \gamma^{\tau-k} L(\tilde{x}_\tau, \tilde{u}_\tau), \quad (12)$$

where  $0 < \gamma \leq 1$ ,  $L(\tilde{x}_\tau, \tilde{u}_\tau) = \tilde{x}_\tau^\top Q \tilde{x}_\tau + \tilde{u}_\tau^\top R \tilde{u}_\tau$  is the cost function,  $Q \succeq 0 \in \mathbb{R}^{n_\kappa \times n_\kappa}$  is positive semi-definite, and  $R \succ 0 \in \mathbb{R}^{n_u \times n_u}$  is positive definite. The second subproblem is how the robot can avoid moving obstacles. Combining the above two subproblems, we formulate the optimal motion planning problem (OMP) as below:

**Problem 1.** (OMP) Design an optimal safe controller for the robot with uncertain system dynamics such that it

- C.1: Starts at  $x_0 \in \mathbb{R}^{n_x}$  and tracks the reference path  $\Xi$  by minimizing the value function  $V_\infty(\tilde{x}_k)$ .
- C.2: Avoids collisions with all obstacles  $\mathcal{B}_1, \dots, \mathcal{B}_q \subseteq \mathcal{W} \subseteq \mathbb{R}^2$ , where  $\mathcal{W}$  denotes the workspace.

#### IV. VECTOR FIELD GUIDED RECEDING HORIZON REINFORCEMENT LEARNING FOR MOBILE ROBOTS WITH UNKNOWN SYSTEM DYNAMICS

It is essential to generate local collision-free trajectories for guiding robots’ motion in obstacle-dense scenarios, which could improve safety and simplify the design of RL dynamic controllers. Motivated by this aspect, we design a guiding vector field that considers dynamic constraints and excludes the deadlock problem (i.e., singular points). This part is illustrated by the *safety guiding module* in Fig. 4. Considering safety when robots track the desired trajectory, we must deal with the movements of (suddenly appearing) moving obstacles and the uncertainties of the nominal deep Koopman model. To this end, we develop an online receding-horizon reinforcement learning (RHRL) approach that employs a game-based exponential barrier function and a fast model compensation scheme. This part is illustrated by the *learning predictive control module* of Fig. 4. The details of each module and its sub-modules will be illustrated in the following subsections.

##### A. Discrete-time Kinodynamic Composite Vector Field

In this subsection, we present a discrete-time kinodynamic composite vector field to generate locally feasible trajectories, corresponding to module A of Fig. 4.

1) *Composite Vector Field with Kinodynamic Constraints:* The first objective in Definition 1 can be achieved by the composite vector field (1). To accomplish the second objective in Definition 1, we first design the following kinodynamic composite vector field based on (1):

$$\begin{aligned} \chi_c(\xi) = & \left( \prod_{i \in \mathcal{I}'} \sqcup_{\mathcal{Q}_i}(\xi) \prod_{i \in \mathcal{I}'} s_i(\xi) \right) \hat{\chi}_{\mathcal{P}}(\xi) \\ & + \sum_{i \in \mathcal{I}'} (\sqcap_{\mathcal{R}_i}(\xi) \hat{\chi}_{\mathcal{R}_i}(\xi)) + \sum_{i \in \mathcal{I}'} (1 - s_i(\xi)) \hat{\chi}_{\mathcal{R}_i}(\xi), \end{aligned} \quad (13)$$

where  $\mathcal{I}'$  is a set containing the index numbers of manually added *virtual obstacles*, and  $s_i : \mathbb{R}^2 \rightarrow \mathbb{R}$  is a function to be designed later. The path generated by the original composite

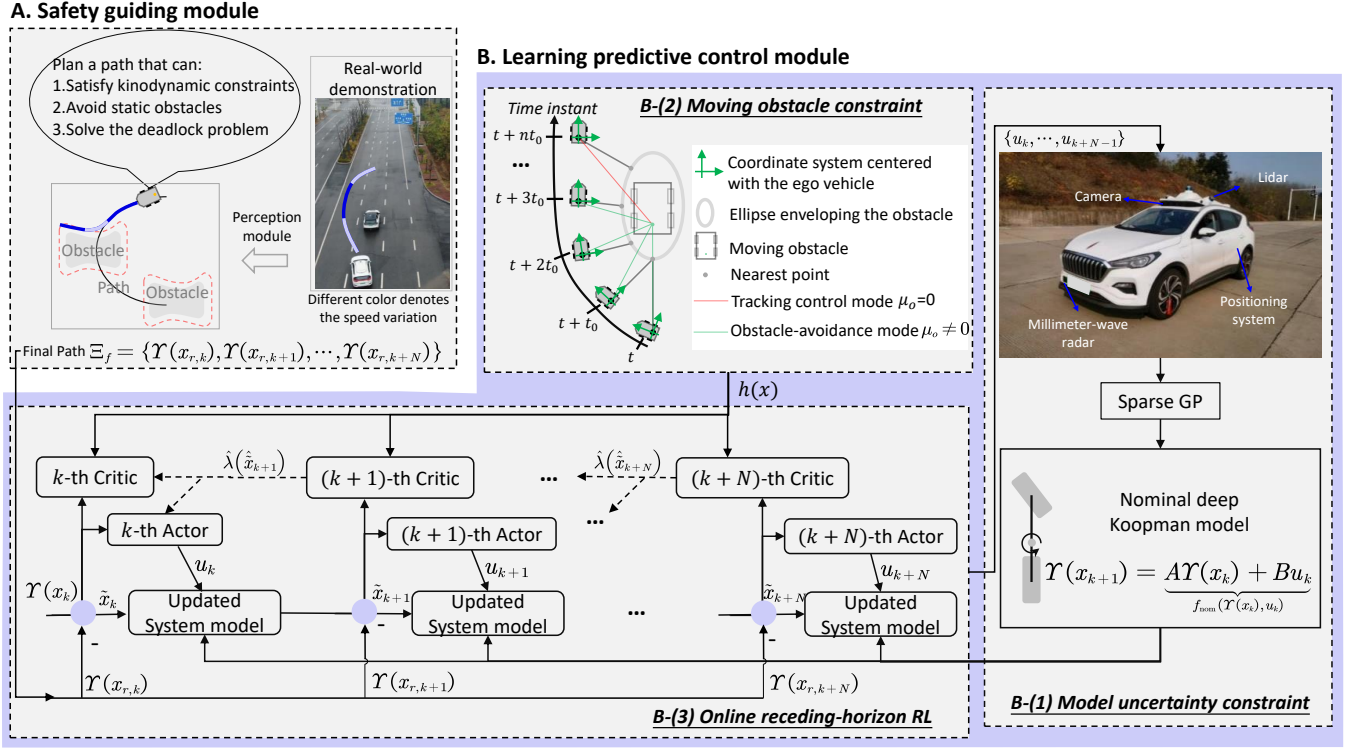


Fig. 4. The overall framework of the VF-LPC algorithm.

vector field in (1) would often require the robot to make large turns within a limited distance for collision avoidance. The role of *virtual obstacles* here is to proactively modify the vector field such that the curvature of the robot trajectory is less than the maximum allowable value as the robot enters the *sandwiched region*

$$\mathcal{M}_s = {}^{\text{ex}}\mathcal{Q}_{\text{actl}} \cap {}^{\text{in}}\mathcal{R}_{\text{actl}}, \quad (14)$$

(i.e., the area sandwiched between the repulsive and the reactive boundaries; see the white annulus region in Fig. 5), thereby satisfying the dynamic constraints. The definitions of the reactive and repulsive boundaries are expressed through the function  $\varphi_i(\xi)$ ,  $i \in \mathcal{I}'$ . For example, the reactive boundary  $\mathcal{R}_{\text{vrtl}}$  corresponding to a virtual obstacle is described by  $\{\xi \in \mathbb{R}^2 : \varphi_i(\xi) = 0\}$ ,  $i \in \mathcal{I}'$  in Fig. 5, and its repulsive boundary  $\mathcal{Q}_{\text{vrtl}}$  is described by  $\{\xi \in \mathbb{R}^2 : \varphi_i(\xi) = c_i\}$ ,  $i \in \mathcal{I}'$ . When the robot's position  $\xi = (X, Y) \in \mathbb{R}^2$  enters the virtual reactive region  ${}^{\text{in}}\mathcal{R}_{\text{vrtl}}$ , it will be attracted towards the virtual repulsive boundary  $\mathcal{Q}_{\text{vrtl}}$ . This provides a direction change before  $\xi$  enters the actual reactive region  ${}^{\text{in}}\mathcal{R}_{\text{actl}}$  corresponding to the actual obstacle, and the virtual obstacle will not affect its motion after  $\xi$  enters the actual reactive region  ${}^{\text{in}}\mathcal{R}_{\text{actl}}$ . Based on the above analyses, within/outside the *buffer region* (i.e., the shaded area in Fig. 5)

$$\mathcal{M}_b = {}^{\text{ex}}\mathcal{R}_{\text{actl}} \cap {}^{\text{in}}\mathcal{R}_{\text{vrtl}}, \quad (15)$$

the function  $s_i(\xi) : \mathbb{R}^2 \rightarrow \mathbb{R}$ ,  $i \in \mathcal{I}'$  is designed to be

$$s_i(\xi) = \begin{cases} \exp\left(\frac{k_{c,i}}{c_i - \varphi_i(\xi)}\right) & \xi \in \mathcal{M}_b, \\ 1 & \text{otherwise,} \end{cases} \quad (16)$$

where the adjustable coefficient  $k_{c,i} > 0$  is used to change the convergence rate to  $\mathcal{Q}_{\text{vrtl}}$ , and  $\exp(\cdot)$  denotes the exponential function. Thus, in this design,  $0 < s_i(\xi) < 1$  if  $\xi \in \mathcal{M}_b$ ;  $s_i(\xi) = 1$ , otherwise.

**Remark 2.** *The placed virtual obstacle is assumed to satisfy  $({}^{\text{in}}\mathcal{Q}_{\text{vrtl}} \cap \mathcal{P}) \subset ({}^{\text{in}}\mathcal{R}_{\text{actl}} \cap \mathcal{P})$ . The assumption is used for letting  $\xi$  exit the sandwiched region  $\mathcal{M}_s$  from  $\mathcal{M}_b$ , but not converging to  $\mathcal{Q}_{\text{vrtl}}$  when robots are in  $\mathcal{M}_b$ .*

**Remark 3.** *Virtual obstacles cease to exert their influence if  $\xi$  enter  $\mathcal{M}_b$  again from  $\mathcal{M}_s$ . This setting stops robots from returning to  $\mathcal{M}_s$ , but enables them to move towards the desired path to complete an obstacle avoidance process.*

Now, the guidance path generated by the vector field  $\chi_c(\xi)$  can avoid rapidly increasing curvature. To satisfy the maximum centripetal acceleration  $a_{\text{max}}$ , *speed planning* is further performed for the path  $\Xi_f = \int_0^T \chi(\xi(t)) dt$  under a given desired speed  $v_d$ , where  $T > 0$  determines the time duration. The maximum allowable speed is  $(a_{\text{max}}/\kappa(t))^{1/2}$ . We can perform *speed planning* by the following strategy: If  $v_d > (a_{\text{max}}/\kappa(t))^{1/2}$ , then set the speed at  $\xi(t)$  to  $(a_{\text{max}}/\kappa(t))^{1/2}$ ; otherwise, set the speed at  $\xi(t)$  to  $v_d$ .

2) *Analysis of the Composite Vector Field:* The composite vector field (13) gives an idea of how to accommodate the kinodynamic constraint. By redesigning the characterizing functions  $\phi$ ,  $\varphi_i$ , the bump functions, and the coefficients  $c_i$ , the first condition of Definition 1 can be met in practice [32]. The second condition can be satisfied by selecting proper positive coefficient  $k_{c,i}$ ,  $i \in \mathcal{I}'$ . These two conditions are satisfied in simulations and experiments in this paper.

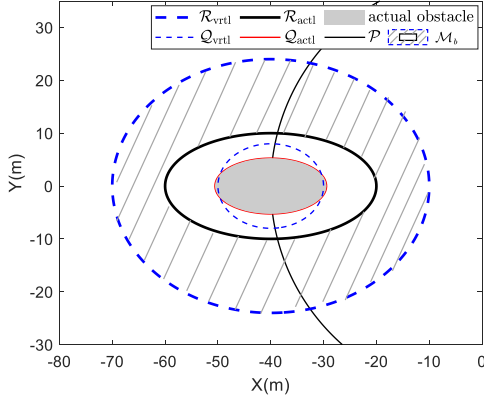


Fig. 5. An illustrative example of the kinodynamic composite vector field. The gray-shaded ellipse is the actual obstacle, and its corresponding repulsive and reactive boundaries are the red and black solid elliptic curves, respectively. The small and large blue circles with dashed lines represent the repulsive and reactive boundaries for a manually added virtual obstacle. The black curve is the desired path.

3) *Discrete-time Kinodynamic Guiding Vector Field*: With  $\chi_c(\xi)$  defined in (13), the desired path is computed by its discrete-time form, i.e.,

$$\xi_{k+1} = \xi_k + \beta \chi_c(\xi_{k,grid}), \quad \xi_0 = (x_0, y_0), \quad (17)$$

where  $\xi_0 \in \mathbb{R}^2$  is the initial robot position and  $\beta$  is the step length, and  $\xi_{k,grid} = \arg \min_{\xi_g \in \mathcal{G}} \|\xi_k - \xi_g\|$ , where the set  $\mathcal{G} \subseteq \mathbb{R}^2$  is the grid map consisting of a finite number of chosen points in a selected region. In terms of computational efficiency, it is advisable to precompute  $\chi_c(\xi)$  on a mesh grid map. This makes it possible to quickly identify the nearest vector  $\chi_c(\xi_{k,grid})$  on the mesh grid map based on the current position  $\xi_k$ . Finally, we can obtain the planned trajectory. Note that a vector with nearly zero norms is not selected as the current vector but rather inherits the vector from the previous state to avoid suffering from the singularity issue. Namely, if  $\|\chi_c(\xi_{k,grid})\| < \epsilon$ , then  $\chi_c(\xi_{k,grid}) \leftarrow \chi_c(\xi_{k-1,grid})$ , where  $\epsilon$  is a small positive number. This allows us to plan guiding trajectories directly without causing the deadlock problem from singular points.

### B. Online Compensation to Update the Offline Trained Deep Koopman Model

In this subsection, we present an online compensation method to update the offline trained deep Koopman model since *model uncertainties* exist. This subsection corresponds to module B-(1) of Fig. 4.

To construct the “input-output” form of a GP, Eq. (9) is rewritten as

$$d(z_k) = B_d^\dagger (\Upsilon(x_{k+1}) - f_{\text{nom}}(\Upsilon(x_k), u_k)), \quad (18)$$

where  $B_d^\dagger$  is the Moore–Penrose pseudoinverse of  $B_d$ .

**Remark 4.** *Due to the necessity for efficient computation in the online compensation of vehicle dynamic models, we further apply the approximate linear dependence (ALD) strategy [9] to quantize the online updated dictionary  $\mathcal{D}_{\text{GP}}$  for obtaining the training dataset  $\mathcal{D}_{\text{SGP}}$ . Note that  $\mathcal{D}_{\text{GP}}$  is obtained in the*

same way as [36]. Subsequently, we employ the Sparse GP-based algorithm FITC [33] for online estimation to enhance the computational efficiency. This approach aligns with our previous work, and additional details can be found in [9].

With the optimized parameters, GP models compensate for model uncertainties. Therefore, we define the learned model of (9) as

$$\Upsilon(x_{k+1}) = f_{\text{nom}}(\Upsilon(x_k), u_k) + d(z_k) + \epsilon, \quad (19)$$

where  $\epsilon \in \mathbb{R}^{n_\kappa}$  is the estimation error. The reference trajectory can be expressed as  $\Upsilon(x_{r,k+1}) = f_{\text{nom}}(\Upsilon(x_{r,k}), u_{r,k})$ .

We can obtain the Jacobian matrix of (19) at a reference state  $(\Upsilon(x_{r,k}), u_{r,k})$ , i.e.,

$$A_{d,k} = A + \frac{\partial d(z_k)}{\partial \Upsilon(x_k)}, B_{d,k} = B + \frac{\partial d(z_k)}{\partial u_k}, \quad (20)$$

where  $A_{d,k} \in \mathbb{R}^{n_\kappa \times n_\kappa}$ ,  $B_{d,k} \in \mathbb{R}^{n_\kappa \times n_u}$ . Note that  $A_{d,k}$  and  $B_{d,k}$  are then used for the training process of model-based RL in Section IV-D. To obtain  $\frac{\partial d(z_k)}{\partial \Upsilon(x_k)}$  and  $\frac{\partial d(z_k)}{\partial u_k}$ , one should compute  $\frac{\partial d(z_k)}{\partial z_k}$  first, which is equivalent to calculating  $\partial (Q_{z_k z_{\text{sp}}} (Q_{z_{\text{sp}} z_{\text{sp}}} + \Lambda)^{-1} \mathbf{y}_{\text{sp}}) / \partial z_k$ , i.e.,

$$\frac{\partial d(z_k)}{\partial z_k} = \frac{1}{\rho^2} (z_{\text{sp}} - [z_k \otimes \mathbf{1}]) (Q_{z_k z_{\text{sp}}} \odot (Q_{z_{\text{sp}} z_{\text{sp}}} + \Lambda)^{-1} \mathbf{y}_{\text{sp}}), \quad (21)$$

where  $z_{\text{sp}} \in \mathbb{R}^{n_z \times n_{\text{sp}}}$  and  $\mathbf{y}_{\text{sp}} \in \mathbb{R}^{n_{\text{sp}} \times n_y}$  denotes the input and output of the training samples  $\mathcal{D}_{\text{SGP}}$ , respectively,  $\mathbf{1}$  denotes an  $n_{\text{sp}}$ -dimensional row vector consisting entirely of 1. Ultimately, this yields matrices  $\frac{\partial d(z_k)}{\partial \Upsilon(x_k)}$  and  $\frac{\partial d(z_k)}{\partial u_k}$ . Then an error model derived from (11) is given below by assuming that the estimation error is sufficiently small, i.e.,

$$\hat{x}_{k+1} = f_{\text{nom}}(\tilde{x}_k, \tilde{u}_k) + d(z_k). \quad (22)$$

### C. Exponential Barrier Function Incorporated Cost Function to Avoid Moving Obstacles

In this subsection, we design a cost function incorporated with an exponential barrier function to deal with the *moving obstacle constraint*, corresponding to module B-(2) of Fig. 4.

Note that C.2 in the OMP Problem can cause safety issues due to the obstacles’ movements. Consistent with [9], an implementable barrier function used for safety is designed as

$$h(x) = \mu_o \exp(-\|\pi(x, x_p)\|), \quad (23)$$

where  $\mu_o \geq 0$  is the penalty coefficient,  $x_p \in \mathbb{R}^2$  is the nearest reactive boundary coordinate from the nearest obstacle, and  $\pi: \mathbb{R}^{n_x} \times \mathbb{R}^2 \rightarrow \mathbb{R}$  maps  $x$  and  $x_p$  to the distance error. With  $h(x)$ , the robot keeps a safe distance from obstacles.

Due to the adoption of rule-based switching between tracking control and obstacle-avoiding modes in [9], without considering obstacle velocities, it does not guarantee the safety of mobile robots under extreme conditions such as the hazardous driving behavior of opposing vehicles. Our idea stems from the work [37] in completing suicidal game tasks. In [37], the “evader” aspires to avoid being caught by the “pursuer” by computing safe actions. Similarly, when moving obstacles obstruct the road ahead, our strategy is to keep a safe distance







Eq. (28) is rewritten by

$$V^{i+1}(\tilde{x}_\tau) = \mathbb{E} \left[ L(\tilde{x}_\tau, \tilde{u}_\tau) + \gamma V^i(\hat{\tilde{x}}_{\tau+1}) \right], \tau \in [k, k+N-1], \quad (29)$$

where the superscript of  $V$  denotes the iteration number.

In alignment with the value function (25), one can derive its finite-horizon form by

$$\lambda(\tilde{x}_\tau) = \partial V(\tilde{x}_\tau) / \partial \tilde{x}_\tau. \quad (30)$$

**Definition 3.** For the critic network, the optimal value function corresponding to the **finite-horizon** optimization objective is defined by  $\partial V^*(\tilde{x}_\tau) / \partial \tilde{x}_\tau$ , i.e.,

$$\lambda^*(\tilde{x}_\tau) = \begin{cases} 2Q\tilde{x}_\tau + \gamma A_{d,\tau}^\top \lambda^*(\hat{\tilde{x}}_{\tau+1}) + \frac{\partial h(x_\tau)}{\partial \tilde{x}_\tau}, & \tau \in [k, k+N-1] \\ 2P\hat{\tilde{x}}_{k+N} + \partial h(x_{k+N}) / \partial \hat{\tilde{x}}_{k+N}, & \tau = k+N \end{cases} \quad (31)$$

With the optimal value function  $\lambda^*(\tilde{x}_\tau)$ , one can compute the optimal control by setting  $\partial V^*(\tilde{x}_\tau) / \partial \tilde{u}(\tilde{x}_\tau) = 0$ . Then, for the actor network, the optimal control corresponding to the **finite-horizon** optimization objective is defined by the following equation:

$$\tilde{u}^*(\tilde{x}_\tau) = u_b \otimes \tanh\left(-\frac{1}{2}\gamma R^{-1} B_{d,\tau}^\top \lambda^*(\hat{\tilde{x}}_{\tau+1})\right), \quad (32)$$

where  $u_b = [u_1, \dots, u_{n_u}]^\top \in \mathbb{R}^{n_u}$  and  $u_1, \dots, u_{n_u}$  denote the maximum values of the corresponding control dimensions, and  $\tanh(\cdot) : \mathbb{R}^{n_u} \rightarrow \mathbb{R}^{n_u}$  is the hyperbolic tangent function.

The optimal control  $\tilde{u}^*(\tilde{x}_\tau)$  and the optimal value function  $\lambda^*(\tilde{x}_\tau)$  are difficult to be solved analytically. This is because  $\lambda^*(\hat{\tilde{x}}_{\tau+1})$  is not available; see Eqs. (31) and (32). However, they can be approximated by two kernel-based structures, which are

$$\hat{\tilde{u}}(\tilde{x}_\tau) = W_{a,\tau}^\top \Phi(\tilde{x}_\tau), \quad (33a)$$

$$\hat{\lambda}(\tilde{x}_\tau) = W_{c,\tau}^\top \Phi(\tilde{x}_\tau), \quad (33b)$$

where  $W_{a,\tau} \in \mathbb{R}^{n_\Phi \times n_u}$  and  $W_{c,\tau} \in \mathbb{R}^{n_\Phi \times n_\kappa}$  are the weights of the actor and critic networks, respectively, and  $n_\Phi$  denotes the dimension of the *RL training* dictionary, which is obtained by employing the ALD strategy [9] to select representative samples from the robot's state space. For the current state  $\tilde{x}_k$ , the basis function in Eq. (33) is constructed by

$$\Phi(\tilde{x}_\tau) = [k(\tilde{x}_\tau, c_1), \dots, k(\tilde{x}_\tau, c_{n_\Phi})]^\top \in \mathbb{R}^{n_\Phi},$$

where  $c_1, \dots, c_{n_\Phi}$  are the elements in the *RL training* dictionary and  $k(\cdot, \cdot) : \mathbb{R}^{n_\kappa} \times \mathbb{R}^{n_\kappa} \rightarrow \mathbb{R}$  is the Gaussian kernel function.

With the estimated value function in (33b) and consistent with (32), we can obtain the target optimal control at the  $\tau$ -th horizon by

$$\tilde{u}(\tilde{x}_\tau) = u_b \tanh\left(-\frac{1}{2}\gamma R^{-1} B_{d,\tau}^\top \hat{\lambda}(\hat{\tilde{x}}_{\tau+1})\right). \quad (34)$$

Note that  $\hat{\tilde{x}}_{\tau+1}$  is obtained by the identified system dynamics (22). Substituting Eq. (33b) into Eq. (31), the target value function becomes

$$\lambda(\tilde{x}_\tau) = \begin{cases} 2Q\tilde{x}_\tau + \gamma A_{d,\tau}^\top \hat{\lambda}(\hat{\tilde{x}}_{\tau+1}) + \frac{\partial h(x_\tau)}{\partial \tilde{x}_\tau}, & \tau \in [k, k+N-1] \\ 2P\hat{\tilde{x}}_{k+N} + \partial h(x_{k+N}) / \partial \hat{\tilde{x}}_{k+N}, & \tau = k+N \end{cases} \quad (35)$$

---

### Algorithm 1: VF-LPC algorithm

---

**Input:** Obstacle states, the ego robot's states, the preliminary reference path.  
**Output:** The optimal control sequence  $\{\tilde{u}_1^*, \tilde{u}_2^*, \dots\}$ .

```

1 Initialize  $W_c, W_a$ ;
2 Function LPC:
3   Initialize the coefficient  $\mu_0$  with 0.
4   if  $(X, Y) \in \mathcal{E}_p$  then
5      $\mu_o \leftarrow$  a positive real number.
6   end
7   for  $i = 1, \dots, i_{\max}$  (maximum iterations) do
8     // Prediction Horizon
9     for  $\tau = k, \dots, k+N$  do
10      Compute  $\hat{\tilde{u}}(\tilde{x}_\tau)$  and  $\hat{\lambda}(\tilde{x}_\tau)$  by Eq. (33).
11      Update the system dynamics (22) and Jacobian matrices (20) with sparse GP.
12      Compute  $\epsilon_c^i(\tilde{x}_\tau)$  and  $\epsilon_a^i(\tilde{x}_\tau)$  with (36) and (37).
13      Update the weights  $W_{c,\tau}$  and  $W_{a,\tau}$  with (38).
14      Apply  $\hat{\tilde{u}}^i(\tilde{x}_\tau)$  to the system (11).
15    end
16    if the weights converge then
17      Obtain the current control policy, and exit.
18    end
19  // Control Horizon
20  Compute the current control  $\hat{\tilde{u}}^i(\tilde{x}_\tau)$  with (33a).
21 Function QuantizedSparseGP:
22   Select a representative sample set  $\mathcal{D}_{\text{SGP}}$  from  $\mathcal{D}_{\text{GP}}$ .
23   Optimize the hyper-parameters for online compensation.
24 end
25 Function Main():
26   while not reaching the destination do
27     Get the current state  $x_0$  of the system.
28     if reaching the end of the guiding trajectory then
29       Obtain the desired trajectory with Eqs. (13) and (17).
30     end
31     if the online dictionary  $\mathcal{D}_{\text{GP}}$  has been collected then
32       Perform QuantizedSparseGP.
33     end
34     Perform LPC and apply  $\hat{\tilde{u}}(\tilde{x}_\tau)$  to the robot.
35   end
36 end

```

---

Next, we present the iterative learning processes. From the previous formulations,  $N$  actor-critic networks are to be constructed to approximate the optimal value function and control in (31) and (32). At the  $i$ -th iteration, the critic network aims at minimizing the error function between the *target* and the *approximate* value functions, which is defined by

$$\epsilon_c^i(\tilde{x}_\tau) = \frac{1}{2} \|\lambda^i(\tilde{x}_\tau) - \hat{\lambda}^i(\tilde{x}_\tau)\|^2. \quad (36)$$

For the actor network, it minimizes the error function between the *target* and the *approximate* controls, which is defined by the following equation:

$$\epsilon_a^i(\tilde{x}_\tau) = \frac{1}{2} \|\tilde{u}^i(\tilde{x}_\tau) - \hat{\tilde{u}}^i(\tilde{x}_\tau)\|^2. \quad (37)$$

Therefore, one can derive the following update rules for the

critic network and the actor network, respectively:

$$W_{c,\tau+1}^i = W_{c,\tau}^i - \eta_c \partial \epsilon_c^i(\tilde{x}_\tau) / \partial W_{c,\tau}^i, \quad (38a)$$

$$W_{a,\tau+1}^i = W_{a,\tau}^i - \eta_a \partial \epsilon_a^i(\tilde{x}_\tau) / \partial W_{a,\tau}^i, \quad (38b)$$

where  $\eta_c, \eta_a > 0$  are the step coefficients of the gradients. At each time instant, the initial weights  $A_\tau$  and  $C_\tau$  inherit from the  $(\tau + 1)$ -th weights of the previous time instant, and  $A_N$  and  $C_N$  inherit from the  $(N - 1)$ -th weights.

The overall algorithm of VF-LPC is shown in Algorithm 1. Also, the convergence theorem of the Eb-RHRL algorithm is given below and its proof is presented in Section V.

**Theorem 1.** (Convergence of the Eb-RHRL). *As the iteration number  $i$  increases, sequences  $\lambda^i$  and  $\tilde{u}^i$  converge to (30) and (32) respectively, i.e., as  $i \rightarrow \infty$ ,  $\lambda^i \rightarrow \lambda^*$  and  $\tilde{u}^i \rightarrow \tilde{u}^*$ .*

Theorem 1 indicates that the Eb-RHRL approach in Algorithm 1 solves the optimal safe control problems under state and control constraints by obtaining the near-optimal solutions.

## V. THEORETIC ANALYSIS

This section presents the theoretical analyses regarding Theorem 1. We prove that the Eb-RHRL algorithm, integrating the game-based barrier function, converges to the optimal value function and control, thereby solving the OMP problem.

The convergence of the finite-horizon adaptive critic learning algorithms has been proved in [41] for deterministic systems, and the work [40] extends it to the stochastic case. Following the line of the above studies, we prove the convergence of the Eb-RHRL algorithm, i.e.,  $\lambda^i \rightarrow \lambda^*$  and  $\tilde{u}^i \rightarrow \tilde{u}^*$  as  $i \rightarrow \infty$ .

**Lemma 1.** *Given a control sequence  $\{\mu^i\}$  involving random actions and taking (24) into (29), one can obtain the following equation:*

$$\Lambda^{i+1}(\tilde{x}_\tau) = \tilde{x}_\tau^\top Q \tilde{x}_\tau + \mu^i(\tilde{x}_\tau)^\top R \mu^i(\tilde{x}_\tau) + h(x_\tau) + \Lambda^i(\hat{x}_{\tau+1}),$$

where  $\mu(\cdot) : \mathbb{R}^{n_\kappa} \rightarrow \mathbb{R}^{n_u}$ . Rewrite (29) as follows:

$$V^{i+1}(\tilde{x}_\tau) = \tilde{x}_\tau^\top Q \tilde{x}_\tau + \tilde{u}^i(\tilde{x}_\tau)^\top R \tilde{u}^i(\tilde{x}_\tau) + h(x_\tau) + V^i(\hat{x}_{\tau+1}),$$

where  $\tilde{u}^i(\tilde{x}_\tau)$  is defined by (34). We can conclude that, if  $V^0(\cdot) = \Lambda^0(\cdot) = 0$ , then  $V^i(\tilde{x}_\tau) \leq \Lambda^i(\tilde{x}_\tau)$  for all  $i$ .

*Proof.* The control sequence  $\{\tilde{u}^i\}$  is used to minimize  $V^i(\tilde{x}_\tau)$ , while all controls in  $\{\mu^i\}$  are randoms. Thus we have  $V^i(\tilde{x}_\tau) \leq \Lambda^i(\tilde{x}_\tau)$ . Under the condition of  $V^0(\cdot) = \Lambda^0(\cdot) = 0$ ,  $V^i(\tilde{x}_\tau) \leq \Lambda^i(\tilde{x}_\tau)$  holds, for all  $i$ .  $\square$

Lemma 1 shows that applying  $\{\tilde{u}^i\}$  to the robot system has a lower value function than the random control sequence. It is now ready to assist in obtaining and proving Lemma 2.

**Lemma 2.** *Let the sequence  $V^i(\tilde{x}_\tau)$  be defined as in (28). By applying an initial admissible control policy, the following conclusions hold: 1) There exists an upper bound  $\bar{Z}(\tilde{x}_\tau)$  such that  $0 \leq V^i(\tilde{x}_\tau) \leq \bar{Z}(\tilde{x}_\tau)$  for all  $i$ . 2) If the optimal control problem (27) is solvable, then there exists an upper bound  $\bar{Z}(\tilde{x}_\tau)$  such that  $V(\tilde{x}_\tau) \leq \bar{Z}(\tilde{x}_\tau)$ , where  $V(\tilde{x}_\tau)$  solves (26) and  $0 \leq V^i(\tilde{x}_\tau) \leq V^*(\tilde{x}_\tau) \leq \bar{Z}(\tilde{x}_\tau)$  for all  $i$ .*

*Proof.* To begin with,  $\eta(\cdot) : \mathbb{R}^{n_\kappa} \rightarrow \mathbb{R}^{n_u}$  is assumed to be an admissible control policy. Let  $V^0(\tilde{x}_\tau) = Z^0(\tilde{x}_\tau) = 0$ , where

$$Z^{i+1}(\tilde{x}_\tau) = \mathbb{E} \left[ L(\tilde{x}_\tau, \eta(\tilde{x}_\tau)) + Z^i(\hat{x}_{\tau+1}) \right]$$

with  $Z^{k+N}(\tilde{x}_\tau) = \mathbb{E} \left( F(\hat{x}_{k+N}) \right)$ , for all  $i \geq 1$ . We define an upper bound

$$\bar{Z}(\tilde{x}_\tau) = \mathbb{E} \left[ \sum_{j=\tau}^{k+N-1} L(\tilde{x}_j, \eta_j(\tilde{x}_j)) + F(\hat{x}_{k+N}) \right],$$

with the dynamic model:  $\hat{x}_{\tau+1} = A_{d,\tau} \tilde{x}_\tau + B_{d,\tau} \eta(\tilde{x}_\tau)$ , where  $L(\tilde{x}_\tau) = \tilde{x}_\tau^\top Q \tilde{x}_\tau + \eta^\top(\tilde{x}_\tau) R \eta(\tilde{x}_\tau) + h(x_\tau)$ . With (28), the following two cases are analyzed, respectively.

*Case 1* ( $\tau + i \leq k + N - 1$ ):

$$\begin{aligned} Z^{i+1}(\tilde{x}_\tau) &= \mathbb{E} \left[ L(\tilde{x}_\tau, \eta(\tilde{x}_\tau)) + Z^i(\hat{x}_{\tau+1}) \right] \\ &= \mathbb{E} \left[ \sum_{j=\tau}^{\tau+1} L(\tilde{x}_j, \eta_j(\tilde{x}_j)) + Z^{i-1}(\hat{x}_{\tau+2}) \right] \\ &\dots \\ &= \mathbb{E} \left[ \sum_{j=\tau}^{\tau+i} L(\tilde{x}_j, \eta_j(\tilde{x}_j)) \right] \end{aligned} \quad (39)$$

Since  $h(\tilde{x}_j) \in \{0, \mu_o\}$ , we have  $L(\tilde{x}_j, \eta_j(\tilde{x}_j)) \geq 0$ . For  $i_1, i_2 \in [k, k + N - 1]$ , one has

$$\sum_{j=\tau}^{\tau+i_1} L(x_j, \eta_j(x_j)) \leq \sum_{j=\tau}^{\tau+i_2} L(x_j, \eta_j(x_j)), i_1 \leq i_2. \quad (40)$$

Combining Eqs. (39) and (40), we have

$$\begin{aligned} Z^{i+1}(\tilde{x}_\tau) &= \mathbb{E} \left[ \sum_{j=\tau}^{\tau+i} L(\tilde{x}_j, \eta_j(\tilde{x}_j)) \right] \\ &\leq \mathbb{E} \left[ \sum_{j=\tau}^{k+N-1} L(\tilde{x}_j, \eta_j(\tilde{x}_j)) + F(\hat{x}_{k+N}) \right] \\ &= \bar{Z}(\tilde{x}_\tau). \end{aligned} \quad (41)$$

*Case 2* ( $\tau + i > k + N - 1$ ):

$$\begin{aligned} Z^{i+1}(\tilde{x}_\tau) &= \mathbb{E} \left[ \sum_{j=\tau}^{k+N-1} L(\tilde{x}_j, \eta_j(\tilde{x}_j)) + Z^{i-(k+N-1-\tau)}(\hat{x}_{k+N}) \right] \\ &= \mathbb{E} \left[ \sum_{j=\tau}^{k+N-1} L(\tilde{x}_j, \eta_j(\tilde{x}_j)) + F(\hat{x}_{k+N}) \right] \\ &= \bar{Z}(\tilde{x}_\tau). \end{aligned} \quad (42)$$

Combining Eqs. (41) and (42),  $Z^{i+1}(\tilde{x}_\tau) \leq \bar{Z}(\tilde{x}_\tau)$  holds.

According to Lemma 1, setting the control sequence  $\{\mu^i\}$  as  $\{\eta^i\}$  and the value function  $\Lambda^i$  as  $Z^i$ , it follows that  $V^i(\tilde{x}_\tau) \leq Z^i(\tilde{x}_\tau) \leq \bar{Z}(\tilde{x}_\tau)$  for all  $i$ , which proves 1). By setting  $\eta = \tilde{u}^*$ ,  $V^i(\tilde{x}_\tau) \leq V^*(\tilde{x}_\tau) \leq \bar{Z}(\tilde{x}_\tau)$  holds, which proves part 2).  $\square$

Under Lemma 2, we now arrive at the proof of Theorem 1.

*Proof of Theorem 1.* According to Lemma 2, as  $i \rightarrow \infty$ ,  $V^i(\tilde{x}_\tau) \rightarrow V^*(\tilde{x}_\tau)$  and  $\tilde{u}^i(\tilde{x}_\tau) \rightarrow \tilde{u}^*(\tilde{x}_\tau)$  hold. Namely,  $\lambda^i(\tilde{x}_\tau)$  in Eq. (35) will converge to  $\lambda^*(\tilde{x}_\tau)$  in Eq. (31).  $\square$

## VI. SIMULATION AND EXPERIMENTAL RESULTS

In this section, we validate our proposed VF-LPC approach (i.e., Algorithm 1) on intelligent vehicles. The algorithm was deployed on a computer running Windows 11 with an Intel Core i7-11800H @2.30GHZ CPU. In the testing scenarios, we compare VF-LPC with several advanced approaches to demonstrate the superiority of VF-LPC. To further verify the effectiveness, we also tested the VF-LPC approach on an actual vehicle of Hongqi EHS-3, shown in the right part of Fig. 4. See the accompanying video for details of the simulation and experiments in this section.

### A. Planning in an Obstacle-Dense Environment

To evaluate the effectiveness of the VF-LPC approach, we compare it with advanced planning approaches in a scenario containing static obstacles; see Fig. 7. We compare VF-LPC with the commonly used planning approaches, such as Hybrid A\* [42], Timed Elastic Bands (TEB) [43] and OBTPAP [44] which iteratively solves the time-optimal motion planning problem. In these tests, we use the analytic kinematic vehicle model with the state variable  $[X, Y, \psi]$ , representing the  $X$ -,  $Y$ -coordinates and the heading, respectively. All the approaches are performed in MATLAB 2023a.

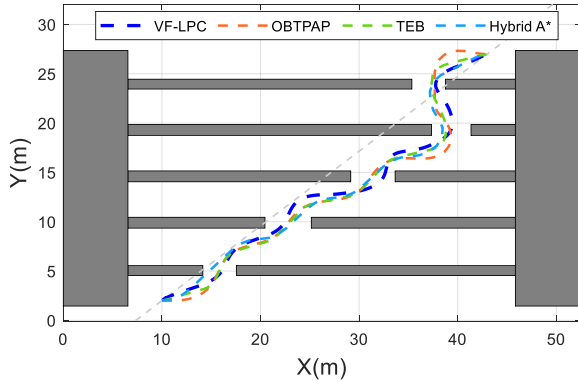


Fig. 7. The planned paths generated by different comparison methods. The gray dotted line is the desired path  $\mathcal{P}$  of VF-LPC.

1) *Evaluation metrics:* To evaluate the planning methods, we employ various performance metrics. The first metric is the path length from the initial point to the destination, denoted as Length; i.e.,  $\text{Length} = \sum_{k=1}^{M-1} \|(X_{k+1}, Y_{k+1}) - (X_k, Y_k)\|$ , where  $M$  is the number of path points. The second metric is Aver. C.T. (average completion time of path planning). The third metric pertains to safety, serving to quantify whether the planned paths meet the collision-free constraint.

TABLE I  
PERFORMANCE EVALUATIONS OF FIG. 7

Quantitative Metrics	VF-LPC	TEB	OBTPAP	Hybrid A*
Length (m)	47.54	47.34	48.44	<b>46.16</b>
Aver. C.T. (s)	<b>0.29</b>	4.80	5.72	2.29
Safety	✓	✓	✓	×

The bold indicates the best result of each metric.

2) *Analyses of the results:* As shown from TABLE I, the paths planned by methods VF-LPC and TEB exhibit similar lengths, albeit shorter than OBTPAP. Though the path length of hybrid A\* is the shortest, it is deemed unsafe due to the lack of maintaining a safe distance while avoiding the first obstacle. Note that VF-LPC is a tracking-avoidance method, while other methods could not demonstrate effectiveness in completing kinodynamic tracking control tasks. Regarding computational efficiency, VF-LPC demonstrates the lowest completion time, measured at 0.29 s, which is significantly lower than those for hybrid A\*, TEB, and OBTPAP.

### B. Collision-Avoidance Simulation in High-Fidelity CarSim

Tracking a desired path while avoiding static and moving obstacles is a fundamental task. To demonstrate the superiority of VF-LPC, we compare it with MPC-CBF [45] and LMPCC [46] under different metrics in MATLAB.

1) *Simulation settings:* All the comparison methods use the system dynamics model (43) and solve the nonlinear optimization problem with the IPOPT solver [47] under CasADi [48]. The vehicle dynamics are described using a “bicycle” model [49] as follows:

$$\begin{bmatrix} \dot{X} \\ \dot{Y} \\ \dot{\psi} \\ \dot{v}_x \\ \dot{v}_y \\ \dot{\omega} \end{bmatrix} = \begin{bmatrix} v_x \cos \psi - v_y \sin \psi \\ v_x \sin \psi + v_y \cos \psi \\ \omega \\ v_y \omega + a_x \\ 2C_{af} \left( \frac{\delta_f}{m} - \frac{v_y + l_f \omega}{m v_x} \right) + 2C_{ar} \frac{l_r \omega - v_y}{m v_x} - v_x \omega \\ \frac{2}{I_z} \left[ l_f C_{af} \left( \delta_f - \frac{v_y + l_f \omega}{v_x} \right) - l_r C_{ar} \frac{l_r \omega - v_y}{v_x} \right] \end{bmatrix}, \quad (43)$$

where  $x = [X, Y, \psi, v_x, v_y, \omega]^T \in \mathbb{R}^6$  is the state vector,  $X, Y$  are the global horizontal and vertical coordinates of the vehicle, respectively,  $\psi$  is the yaw angle,  $v_x, v_y$  denote the longitudinal and lateral velocities, respectively,  $\omega$  denotes the yaw rate,  $l_f$  and  $l_r$  are the distances from the center of gravity (CoG) to the front and rear wheels, respectively;  $C_{af}, C_{ar}$  represent the cornering stiffnesses of the front and rear wheels, respectively;  $I_z$  denotes the yaw moment of inertia;  $m$  is the vehicle’s mass. Their values can be found in TABLE II. In this model, the acceleration  $a_x$  and the steering angle  $\delta_f$  are two variables of the control vector  $u$ , i.e.,  $u = [a_x, \delta_f]^T$ . The reference state is  $x_r = [X_r, Y_r, \psi_r, v_x^r, v_y^r, \omega_r]^T$ .

TABLE II  
VEHICLE DYNAMIC PARAMETERS

$m$	$I_z$	$l_f$	$l_r$	$C_{af}$	$C_{ar}$
2257kg	3524.9kg · m <sup>2</sup>	1.33m	1.81m	66900N/rad	62700N/rad

For VF-LPC, we employed the approach outlined in [23] to conduct system identification by collecting vehicle motion data from the CarSim solver. Finally, a linear time-invariant system model (4) is generated for the VF-LPC algorithm, where  $n_{\mathcal{K}} = 10$  and  $n_u = 2$ . To construct an error model for facilitating subsequent algorithm design, we subtract the desired state from the current state, i.e.,  $\tilde{x} = x - x_r$  and the desired control from system control, i.e.,  $\tilde{u} = u - u_r = [a_x, \delta_f]^T$ .

2) *Evaluation metrics*: The desired speed  $v_d$  of all the methods is set to 25 km/h. To evaluate the VF-LPC approach, we compare it with other safe motion control algorithms under several metrics, which are Aver. S.T. (average solution time of each time step),  $J_{\text{Lat}}$  (cost of the lateral error),  $J_{\text{Heading}}$  (cost of the heading error), and  $J_{\text{Con}}$  (control cost). We define a weighted average metric to evaluate the overall performance, which is

$$J_{\text{MC}} = \frac{1}{M} \sum_{k=1}^M (Q_1 J_{k,\text{Lat}} + Q_2 J_{k,\text{Heading}} + J_{k,\text{Con}}),$$

where  $J_{\text{Lat}} = \|e_y\|^2$ ,  $J_{\text{Heading}} = \|e_\psi\|^2$ ,  $J_{\text{Con}} = \tilde{u}^T R \tilde{u}$  is the control cost, and  $M$  is the number of waypoints of the planned path. Another two quantitative metrics are the overall path length  $\text{Length} = \sum_{k=1}^{M-1} \|(X_{k+1}, Y_{k+1}) - (X_k, Y_k)\|$  and the completion time taken by different methods, i.e., CT.

3) *Analyses of the results*: The testing scenario requires the vehicle to track a reference path (black line in Fig. 8) while avoiding collisions with static and moving obstacles.

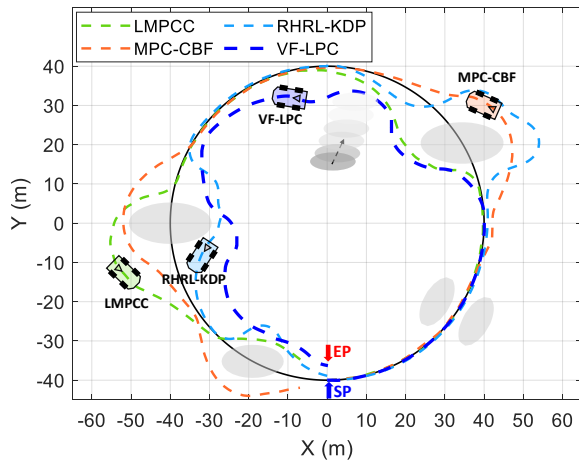


Fig. 8. Simulation results of avoiding static and moving obstacles for four methods. The black arrow denotes the moving direction of the dynamic obstacle, and the black thin line is the desired path. Labels ‘EP’ and ‘SP’ denote the endpoint and start point, respectively.

TABLE III  
PERFORMANCE EVALUATIONS OF FIG. 8

Quantitative Metrics	VF-LPC	MPC-CBF	LMPCC	RHRL-KDP
$J_{\text{MC}}$	<b>62.12</b>	69.34	80.79	121.20
CT (s)	<b>34.05</b>	40.00	37.55	42.78
Length (m)	<b>239.54</b>	278.27	262.83	283.99
Aver. S.T. (s)	<b>0.05</b>	0.09	0.10	0.09

The bold indicates the best result of each metric.

As seen in TABLE III, VF-LPC has the lowest motion control cost  $J_{\text{ML}}$ . The computational cost of VF-LPC is lower

than that of MPC-CBF, LMPCC and RHRL-KDP, and it generates the shortest path. As VF-LPC employs a linear time-invariant Koopman-based vehicle dynamic model to optimize the nonlinear optimal motion planning problem based on the scheme of Eb-RHRL, the computational time is the least. However, the MPC-based methods and RHRL-KDP require online solving of nonlinear optimization problems, resulting in a greater computational burden.

The adopted deep Koopman model is designed for real-time optimal planning and control of intelligent vehicles. Therefore, we demonstrate its effectiveness by showcasing the position and velocity error between the vehicle and the reference path during the task completion process. The simulation results are illustrated in Fig. 9. As depicted in the upper subfigure, within the obstacle-free region (0-70 m), the vehicle exhibits minimal velocity deviation, even when encountering obstacles with a reduction in velocity due to velocity planning. After avoiding the obstacle, the vehicle quickly regains its desired velocity. In the bottom subfigure, within the obstacle-free region, the vehicle demonstrates a minor tracking error (about 0.1m) in following the desired path. This observation underscores the VF-LPC’s commendable safety control performance.

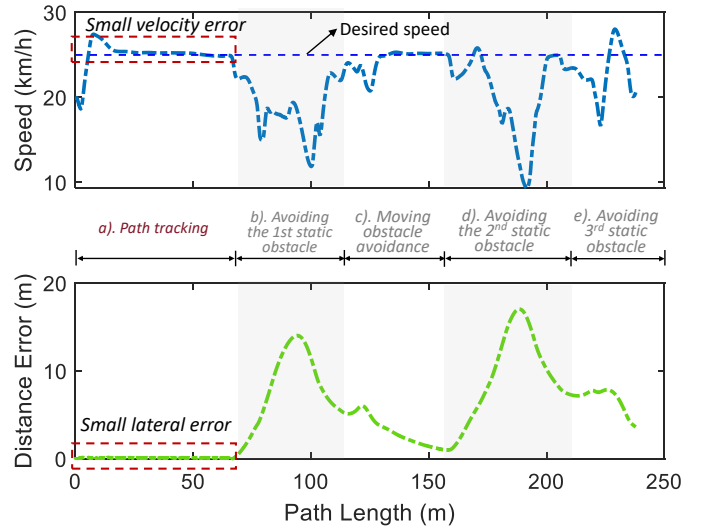


Fig. 9. The vehicle speed and distance error from the desired path of VF-LPC. The red dashed line at the upper panel represents the desired speed of 25 km/h, and the blue solid line represents the speed of the vehicle. The bottom panel presents the distance error between the vehicle and the reference path.

### C. Model Uncertainties Learning

As mentioned in previous sections, the offline trained deep Koopman model probably does not perfectly reflect the exact system dynamics when deployed online due to external uncertainties. As a result, this could cause performance degradation both in planning and control and even safety issues. In this section, we will demonstrate the sparse GP-based learning model uncertainties for the deep Koopman model.

The uncertainty in the dynamics of a system negatively affects the planning and control performance of robots. To eliminate the influence, a quantified sparse GP [9] is utilized to compensate for the difference between the offline-trained deep



Koopman model and the exact vehicle model. The simulated dynamical model can be derived from Eq. (43), revealing that the vehicle states  $v_x, v_y, \omega$  and  $\rho_e(x_k)$  are primarily affected by dynamic parameters. Therefore, we further derive

$$B_d = [\mathbf{0}_3 \ I_3 \ \mathbf{0}_{3 \times n_{\rho_e}}]^\top,$$

$$\text{and } g(x, u) = g(v_x, v_y, \omega, \rho_e^\top, a_x, \delta_f) : \mathbb{R}^{n_{\rho_e} + 5} \rightarrow \mathbb{R}^3.$$

The algorithm was simulated in a racing track road and the desired speed  $v_d$  is set to be 6m/s. Note that we collect motion data of the real vehicle (right half of Fig. 4) to train for an offline nominal deep Koopman model with  $n_{\rho_e} = 6$  and  $x = [X, Y, \psi, v_x, v_y, \omega]^\top \in \mathbb{R}^6$ . The exact vehicle parameters are:  $m = 1257\text{kg}$ ,  $I_z = 1524.9\text{kg} \cdot \text{m}^2$ ,  $C_{af} = 8790\text{N/rad}$ , and  $C_{ar} = 30400\text{N/rad}$ . The iid process noise  $w_k \in \mathbb{R}^6$  with zero mean and variance  $\sigma = 0.002$  is added to the vehicle dynamics. Specifically,  $g(x, u)$  maps  $[x, u]^\top$  to  $[v_x, v_y, \omega]^\top$ .

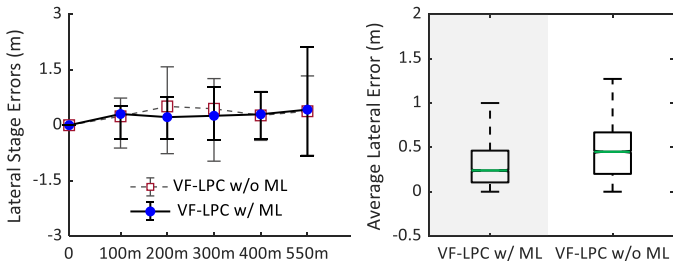


Fig. 10. Tracking error comparison between VF-LPC (w/o ML) and VF-LPC (w/ ML).

To evaluate the effectiveness of our algorithm on learning model uncertainties, VF-LPC with and without model learning, abbreviated as VF-LPC (w/ ML) and VF-LPC (w/o ML), are separately tested on the racing road. At the initial stage, i.e., the first 100m, we update the dictionary online, and it is then sparsified with Approximate Linear Dependence (ALD) similarly to [9]. With the sparsified dictionary, we train it to update the Jacobian matrices (20) and compensate for (4) during the remaining miles.

From the simulation results in Fig. 10, notable improvement can be observed in the lateral stage error of VF-LPC (w/ ML) compared to VF-LPC (w/o ML). Ultimately, the average lateral error throughout the entire testing process for VF-LPC (w/ ML) is lower than that of VF-LPC (w/o ML). These results validate the capability of VF-LPC to process model uncertainty and enhance control performance.

#### D. Real-World Experiments

To further validate the effectiveness of VF-LPC, real-world vehicular experiments were conducted on the Hongqi E-HS3 platform, which is shown in module B-(1) of Fig. 4.

At each time instance within the predictive horizon, the desired trajectory and obstacles are initially transformed into the vehicle body's local coordinate system. Then, we employ polynomial curves to fit the desired path points, obtaining the desired path  $\mathcal{P}$  with (13). Subsequently, the safe trajectory generated by the kinodynamic composite vector field is transformed back into the global coordinate system.

1) *Multiple Static Obstacles Avoidance*: In this scenario, we evaluate the obstacle avoidance capability of the VF-LPC approach. As illustrated in Fig. 11, the black dash line denotes the desired path. Due to the vehicle's long wheelbase of 4.9 meters, the turning radius is large. However, the desired path is constrained and small in size, posing a significant challenge for the algorithm in terms of safe obstacle avoidance and tracking. We set the speed to 1.5m/s, and it can be observed that the vehicle successfully reaches the destination while avoiding multiple obstacles. VF-LPC can plan a smooth trajectory for guiding finite-horizon actor-critic learning processes. This also reflects the effectiveness and advantages of the kinodynamic guiding vector field which satisfies the kinodynamic constraint.

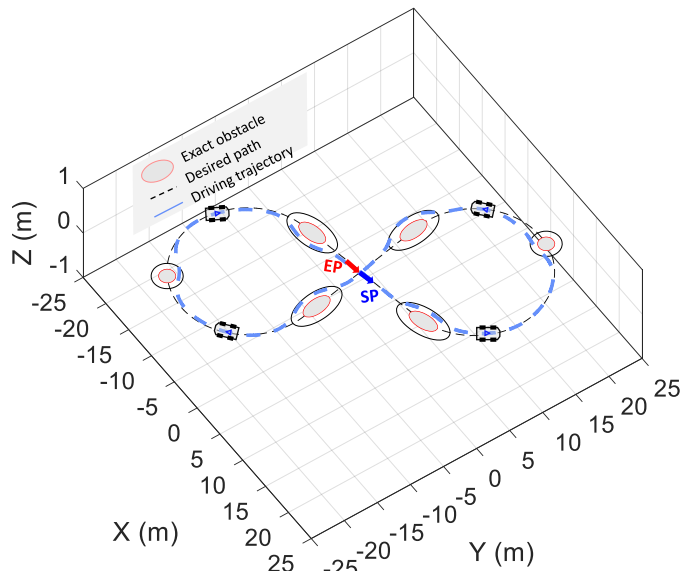


Fig. 11. Avoiding multiple static obstacles when tracking a size-constrained desired path. The black vehicles represent the intelligent vehicle at different time instants. Labels 'EP' and 'SP' denote the endpoint and starting point.

2) *Moving Obstacles Avoidance*: As shown in Fig. 12, a human driver first drove the intelligent vehicle to generate the desired path  $\mathcal{P}$  in this scenario. We have the following settings for testing our algorithm: The moving obstacles start to move at different preset velocities when the distance between them and the intelligent vehicle is less than 25m, thereby validating its emergency collision avoidance capability. Using a gradient of gray, we label the obstacles' positions at different moments during their motion processes, where the darkest color represents the initial moment.

From the overall tracking results in Fig. 12, the intelligent vehicle keeps safe distances from obstacles all the time and returns to the desired path smoothly. In addition, our method exhibits small lateral tracking errors and longitudinal velocity deviation. Moreover, the maximum vehicle's speed reaches 2.4 m/s. Finally, it arrives at the ending point successfully and completes the safe tracking control task.

## VII. CONCLUSION AND FUTURE WORK

This paper presents the Vector Field-guided Learning Predictive Control (VF-LPC) approach for mobile robots with

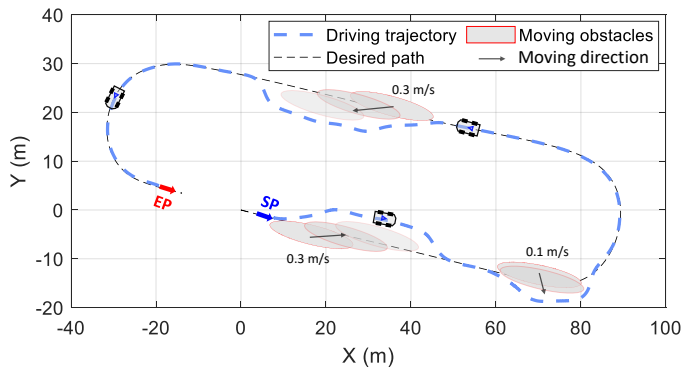


Fig. 12. Avoiding multiple moving obstacles when tracking a desired path. The vehicles represent the intelligent vehicle in different time instants. Labels 'EP' and 'SP' denote the endpoint and start point, respectively.

safety guarantees, which offers a framework for integrated planning and tracking control of robots. VF-LPC incorporates robot dynamics constraints into the guiding vector field for safe robot maneuvering. This is a notable improvement over the existing composite vector fields. Also, the system dynamics are unknown and are learned using the deep Koopman operator. This learned model is then updated online by sparse GP to improve safety and control performance. In addition, VF-LPC guarantees safety by transforming the safety problem into the pursuit-evasion game between a pursuer and an evader; thus, a game-based exponential barrier function is proposed, and a nonlinear optimal control problem is optimized and solved within the receding-horizon RL framework. A rigorous theoretical analysis of Eb-RHRL is provided to guarantee online convergence of learning optimal policies. Extensive simulations and real-world experiments validate the superiority of the proposed VF-LPC approach.

Our work has several possible future directions. 1) VF-LPC is effective in collision-avoidance tests. Under an added prediction module, we believe that VF-LPC could be promising even in higher-speed tasks. 2) In unknown environments, it is still challenging to obtain prior information on obstacles, such as positions and contours. One may need to construct safe barrier functions in real-time using the sensor-perceived information. 3) The effectiveness of VF-LPC has been validated through real-world experiments. Future work could investigate and deploy VF-LPC on more complex dynamic systems.

## REFERENCES

- [1] W. Yao, H. G. de Marina, B. Lin, and M. Cao, "Singularity-free guiding vector field for robot navigation," *IEEE Transactions on Robotics*, vol. 37, no. 4, pp. 1206–1221, 2021.
- [2] N. Slegers and C. Gorman, "Comparison and analysis of multi-body parafoil models with varying degrees of freedom," in *21st AIAA Aerodynamic Decelerator Systems Technology Conference and Seminar*, 2011, p. 2615.
- [3] A. H. D. Nunes, G. V. Raffo, and L. C. A. Pimenta, "Integrated vector field and backstepping control for quadcopters," in *2023 IEEE International Conference on Robotics and Automation (ICRA)*, 2023, pp. 1256–1262.
- [4] Y. A. Kapitanyuk, A. V. Proskurnikov, and M. Cao, "A guiding vector-field algorithm for path-following control of nonholonomic mobile robots," *IEEE Transactions on Control Systems Technology*, vol. 26, no. 4, pp. 1372–1385, 2018.

- [5] W. Yao, *Guiding vector fields for robot motion control*. Springer Nature, 2023, vol. 154.
- [6] V. M. Goncalves, L. C. Pimenta, C. A. Maia, B. C. Dutra, and G. A. Pereira, "Vector fields for robot navigation along time-varying curves in  $n$ -dimensions," *IEEE Transactions on Robotics*, vol. 26, no. 4, pp. 647–659, 2010.
- [7] D. A. Lawrence, E. W. Frew, and W. J. Pisano, "Lyapunov vector fields for autonomous unmanned aircraft flight control," *Journal of Guidance, Control, and Dynamics*, vol. 31, no. 5, pp. 1220–1229, 2008.
- [8] C. Lian, X. Xu, H. Chen, and H. He, "Near-optimal tracking control of mobile robots via receding-horizon dual heuristic programming," *IEEE Transactions on Cybernetics*, vol. 46, no. 11, pp. 2484–2496, 2015.
- [9] Y. Lu, X. Zhang, X. Xu, and W. Yao, "Learning-based near-optimal motion planning for intelligent vehicles with uncertain dynamics," *IEEE Robotics and Automation Letters*, vol. 9, no. 2, pp. 1532–1539, 2024.
- [10] X. Zhang, Y. Jiang, Y. Lu, and X. Xu, "Receding-horizon reinforcement learning approach for kinodynamic motion planning of autonomous vehicles," *IEEE Transactions on Intelligent Vehicles*, vol. 7, no. 3, pp. 556–568, 2022.
- [11] B. A. H. Vicente, S. S. James, and S. R. Anderson, "Linear system identification versus physical modeling of lateral-longitudinal vehicle dynamics," *IEEE Transactions on Control Systems Technology*, vol. 29, no. 3, pp. 1380–1387, 2020.
- [12] T. Gräber, S. Lupberger, M. Unterreiner, and D. Schramm, "A hybrid approach to side-slip angle estimation with recurrent neural networks and kinematic vehicle models," *IEEE Transactions on Intelligent Vehicles*, vol. 4, no. 1, pp. 39–47, 2019.
- [13] N. A. Spielberg, M. Brown, N. R. Kapania, J. C. Kegelman, and J. C. Gerdes, "Neural network vehicle models for high-performance automated driving," *Science Robotics*, vol. 4, no. 28, p. eaaw1975, 2019.
- [14] M. Da Lio, D. Bortoluzzi, and G. P. Rosati Papini, "Modelling longitudinal vehicle dynamics with neural networks," *Vehicle System Dynamics*, vol. 58, no. 11, pp. 1675–1693, 2020.
- [15] P. J. Schmid, "Dynamic mode decomposition of numerical and experimental data," *Journal of Fluid Mechanics*, vol. 656, pp. 5–28, 2010.
- [16] M. O. Williams, I. G. Kevrekidis, and C. W. Rowley, "A data-driven approximation of the koopman operator: Extending dynamic mode decomposition," *Journal of Nonlinear Science*, vol. 25, pp. 1307–1346, 2015.
- [17] I. Kevrekidis, C. W. Rowley, and M. Williams, "A kernel-based method for data-driven koopman spectral analysis," *Journal of Computational Dynamics*, vol. 2, no. 2, pp. 247–265, 2016.
- [18] X. Zhang, W. Pan, R. Scattolini, S. Yu, and X. Xu, "Robust tube-based model predictive control with koopman operators," *Automatica*, vol. 137, p. 110114, 2022.
- [19] Q. Li, F. Dietrich, E. M. Bollt, and I. G. Kevrekidis, "Extended dynamic mode decomposition with dictionary learning: A data-driven adaptive spectral decomposition of the koopman operator," *Chaos: An Interdisciplinary Journal of Nonlinear Science*, vol. 27, no. 10, 2017.
- [20] B. Lusch, J. N. Kutz, and S. L. Brunton, "Deep learning for universal linear embeddings of nonlinear dynamics," *Nature communications*, vol. 9, no. 1, p. 4950, 2018.
- [21] S. E. Otto and C. W. Rowley, "Linearly recurrent autoencoder networks for learning dynamics," *SIAM Journal on Applied Dynamical Systems*, vol. 18, no. 1, pp. 558–593, 2019.
- [22] Y. Xiao, X. Zhang, X. Xu, X. Liu, and J. Liu, "Deep neural networks with koopman operators for modeling and control of autonomous vehicles," *IEEE Transactions on Intelligent Vehicles*, vol. 8, no. 1, pp. 135–146, 2022.
- [23] Y. Xiao, X. Zhang, X. Xu, Y. Lu, and J. Li, "DDK: A deep koopman approach for longitudinal and lateral control of autonomous ground vehicles," in *2023 IEEE International Conference on Robotics and Automation (ICRA)*. IEEE, 2023, pp. 975–981.
- [24] L. Blackmore, M. Ono, and B. C. Williams, "Chance-constrained optimal path planning with obstacles," *IEEE Transactions on Robotics*, vol. 27, no. 6, pp. 1080–1094, 2011.
- [25] B. Luders, M. Kothari, and J. How, "Chance constrained rrt for probabilistic robustness to environmental uncertainty," in *AIAA Guidance, Navigation, and Control Conference*, 2010, p. 8160.
- [26] G. S. Aoude, B. D. Luders, J. M. Joseph, N. Roy, and J. P. How, "Probabilistically safe motion planning to avoid dynamic obstacles with uncertain motion patterns," *Autonomous Robots*, vol. 35, pp. 51–76, 2013.
- [27] L. Lindemann, M. Cleaveland, Y. Kantaros, and G. J. Pappas, "Robust motion planning in the presence of estimation uncertainty," in *2021 60th IEEE Conference on Decision and Control (CDC)*. IEEE, 2021, pp. 5205–5212.

- [28] A. Dixit, M. Ahmadi, and J. W. Burdick, "Risk-sensitive motion planning using entropic value-at-risk," in *2021 European Control Conference (ECC)*. IEEE, 2021, pp. 1726–1732.
- [29] A. Dixit, M. Ahmadi, and J. W. Burdick, "Risk-averse receding horizon motion planning for obstacle avoidance using coherent risk measures," *Artificial Intelligence*, vol. 325, p. 104018, 2023.
- [30] C. Diehl, T. S. Sievernich, M. Krüger, F. Hoffmann, and T. Bertram, "Uncertainty-aware model-based offline reinforcement learning for automated driving," *IEEE Robotics and Automation Letters*, vol. 8, no. 2, pp. 1167–1174, 2023.
- [31] S. Wang, R. Gao, R. Han, S. Chen, C. Li, and Q. Hao, "Adaptive environment modeling based reinforcement learning for collision avoidance in complex scenes," in *2022 IEEE/RSJ International Conference on Intelligent Robots and Systems (IROS)*, 2022, pp. 9011–9018.
- [32] W. Yao, B. Lin, B. D. Anderson, and M. Cao, "Guiding vector fields for following occluded paths," *IEEE Transactions on Automatic Control*, vol. 67, no. 8, pp. 4091–4106, 2022.
- [33] E. Snelson and Z. Ghahramani, "Sparse gaussian processes using pseudo-inputs," *Advances in Neural Information Processing Systems*, vol. 18, 2005.
- [34] C. E. Rasmussen, "Gaussian processes in machine learning," in *Summer School on Machine Learning*. Springer, 2003, pp. 63–71.
- [35] L. Hewing, J. Kabzan, and M. N. Zeilinger, "Cautious model predictive control using gaussian process regression," *IEEE Transactions on Control Systems Technology*, vol. 28, no. 6, pp. 2736–2743, 2019.
- [36] J. Kabzan, L. Hewing, A. Liniger, and M. N. Zeilinger, "Learning-based model predictive control for autonomous racing," *IEEE Robotics and Automation Letters*, vol. 4, no. 4, pp. 3363–3370, 2019.
- [37] I. Exarchos, P. Tsiotras, and M. Pachter, "On the suicidal pedestrian differential game," *Dynamic Games and Applications*, vol. 5, pp. 297–317, 2015.
- [38] J. Liu, Z. Huang, X. Xu, X. Zhang, S. Sun, and D. Li, "Multi-kernel online reinforcement learning for path tracking control of intelligent vehicles," *IEEE Transactions on Systems, Man, and Cybernetics: Systems*, vol. 51, no. 11, pp. 6962–6975, 2021.
- [39] Y. Lu, W. Li, X. Zhang, and X. Xu, "Continuous-time receding-horizon reinforcement learning and its application to path-tracking control of autonomous ground vehicles," *Optimal Control Applications and Methods*, 2021.
- [40] X. Xu, H. Chen, C. Lian, and D. Li, "Learning-based predictive control for discrete-time nonlinear systems with stochastic disturbances," *IEEE Transactions on Neural Networks and Learning Systems*, vol. 29, no. 12, pp. 6202–6213, 2018.
- [41] A. Heydari and S. N. Balakrishnan, "Finite-horizon input-constrained nonlinear optimal control using single network adaptive critics," in *Proceedings of the 2011 American Control Conference*, 2011, pp. 3047–3052.
- [42] D. Dolgov, S. Thrun, M. Montemerlo, and J. Diebel, "Practical search techniques in path planning for autonomous driving," *Ann Arbor*, vol. 1001, no. 48105, pp. 18–80, 2008.
- [43] C. Rösmann, W. Feiten, T. Wösch, F. Hoffmann, and T. Bertram, "Trajectory modification considering dynamic constraints of autonomous robots," in *ROBOTIK 2012; 7th German Conference on Robotics*. VDE, 2012, pp. 1–6.
- [44] B. Li, T. Acarman, Y. Zhang, Y. Ouyang, C. Yaman, Q. Kong, X. Zhong, and X. Peng, "Optimization-based trajectory planning for autonomous parking with irregularly placed obstacles: A lightweight iterative framework," *IEEE Transactions on Intelligent Transportation Systems*, vol. 23, no. 8, pp. 11 970–11 981, 2021.
- [45] J. Zeng, B. Zhang, and K. Sreenath, "Safety-critical model predictive control with discrete-time control barrier function," in *American Control Conference (ACC)*, 2021, pp. 3882–3889.
- [46] B. Brito, B. Floor, L. Ferranti, and J. Alonso-Mora, "Model predictive contouring control for collision avoidance in unstructured dynamic environments," *IEEE Robotics and Automation Letters*, vol. 4, no. 4, pp. 4459–4466, 2019.
- [47] A. Wächter and L. T. Biegler, "On the implementation of an interior-point filter line-search algorithm for large-scale nonlinear programming," *Mathematical programming*, vol. 106, no. 1, pp. 25–57, 2006.
- [48] J. A. Andersson, J. Gillis, G. Horn, J. B. Rawlings, and M. Diehl, "CasADi: a software framework for nonlinear optimization and optimal control," *Mathematical Programming Computation*, vol. 11, no. 1, pp. 1–36, 2019.
- [49] R. Rajamani, *Vehicle dynamics and control*. Springer Science & Business Media, 2011.